Microgravity containerless processing – rapid solidification

Authors:

D.M. Matson(1), L. Battezzati(2), P.K. Galenko(3), Ch.-A. Gandin (4), A.K. Gangopadhyay(5), H. Henein(6), K.F. Kelton(5), M. Kolbe(7), J. Valloton(6), S.C. Vogel(8), T. Volkmann(7)

Correspondence: Douglas Matson (douglas.matson@tufts.edu)

Institutions:

1 Department of Mechanical Engineering, Tufts University, Medford MA 02155 USA

2 Dipartimento di Chimica e Centro NIS, Università di Torino, Via P. Giuria 7, 10125 Torino, Italy

3 Otto-Schott-Institut für Materialforschung, Friedrich Schiller Universität Jena, Jena, Germany

4 MINES Paris, PSL University, CEMEF UMR 7635, CS10207, 06904 Sophia Antipolis, France

5 Department of Physics and the Institute of Materials Science & Engineering, Washington University, St. Louis, MO 63130-4899, USA

6 Department of Chemical and Materials Engineering, University of Alberta, Edmonton, Alberta, Canada T6G 2G6

7 Institut für Materialphysik im Weltraum, Deutsches Zentrum für Luft- und Raumfahrt (DLR), 51170 Köln, Germany.

8 Materials Science and Technology Division, Los Alamos National Laboratory, Los Alamos NM 87545 USA

ABSTRACT

Space levitation processing allows researchers to conduct benchmark tests in an effort to understand the physical phenomena involved in rapid solidification processing including alloy thermodynamics, nucleation and growth, heat and mass transfer, solid/liquid interface dynamics, macro- and microstructural evolution, and defect formation. Supported by ground-based investigations, a major thrust is to develop and refine robust computational tools based on theoretical and applied approaches. This work is accomplished in conjunction with experiments designed for precise model validation with application to a broad range of industrial processes.

INTRODUCTION

The quantitative and predictive modelling of liquid-state manufacturing processes is now a cornerstone of current engineering projects, starting from alloy selection to solidification-process design, evolution of the solidification macro- and microstructure, and subsequent thermomechanical treatments to achieve optimum mechanical properties. [1] This includes not only the processes for semi-finished products and shape castings, but also processes entailing

rapid solidification such as high-pressure die casting, strip casting, welding, atomization, spray forming and additive manufacturing (3D printing). Of particular interest is developing computational tools, in conjunction with model validation testing[2], to aid in the control of rapid solidification processes.

These issues cover the whole range from optimized solidification techniques to tailoring of the solidification microstructure, combined with optimization of the alloy composition and development of new alloy compositions for a given application – all with an eye to supporting closed-loop recycling. The approach is relevant for all cast products and alloys, ranging from the automotive world, turbine blades for land-based energy production and jet engines, medical implants, large- and small-scale casting, and semi-finished products such as the continuous casting of slabs. In recent years, its high relevance for additive manufacturing processes has also become particularly significant.

Containerless processing, both on ground and in a microgravity environment, is particularly important for conducting benchmark experiments to support solidification physics research topics – particularly for investigations targeting evaluation of phase selection and microstructural evolution following rapid solidification from the undercooled melt and subsequent mushy-zone microstructural evolution. For space testing, an electromagnetic levitation facility (ISS-EML) was developed to enable transformative molten metal and rapid solidification experimentation in the microgravity environment of the International Space Station (ISS) [3]. The key attributes for space testing include limiting the influence of buoyancy and sedimentation, maintaining a spherical equilibrium sample shape during levitation to simplify the analysis of processing conditions under dynamic stimulation, and accessing controlled convection conditions which span the range from laminar flow to turbulent flow with the ability to select conditions that optimize scientific return from a particular set of experiment design consider

ations. Obviously, close collaboration is required with groups conducting thermophysical property measurement to enable researchers to select and control convection to the specified desired levels for a given test.

DISCUSSION

Space research on rapid solidification focuses on key topics which include: structure of metallic melts, influence of convection on nucleation, influence of convection on metastable phase selection, growth competition kinetics, atomization, evaluation of the solidification path for multi-component systems, anomalous growth kinetics, directional solidification, grain refinement, and demixing of liquids and solids.

Relation between Dynamics and Structure in Metallic Liquids.

The viscosity changes by over sixteen orders of magnitude from the value at the melting (or liquidus) temperature, T_L, to that at the glass transition temperature (the point at which the liquid becomes a glass), T_g. As first suggested by Angell [4], the rate of this change can be expressed in terms of the *fragility* of the liquid. In a *strong* liquid, the temperature dependence of the viscosity is nearly Arrhenius over the temperature range. As the temperature dependence departs from an Arrhenius one, the liquid becomes more *fragile*. This is generally expressed by the fragility index,

$$m = d(\log_{10}\eta) \Big/ d\left(T_g / T\right)\Big|_{T_g} . \qquad (1)$$

Fragility has also been identified in the temperature dependence of other physical quantities, such as the entropy [5], specific heat [6], mechanical properties of glasses [7] and in the rate of structural ordering in the liquid [8] This suggests that there must be a deep link between the structure of the liquid and its dynamical behavior [9-10].

While molecular dynamics (MD) investigations of structural/dynamical correlations give questionable results near T_g because of the vastly different relaxation times between the simulations and experiments, they can be used to study the high temperature liquid where the relaxation rates are comparable. Based on MD studies of metallic liquids, fluctuations in the local atomic structure (characterized by the time that it takes for a local cluster to change its coordination number by one, τ_{LC}) can be correlated with dynamical behavior [11-14]. At high temperatures the lifetime of these local structural fluctuations is too short to have an impact on nearby regions. However, below a material-dependent temperature, T_A, the lifetime becomes sufficiently long that local fluctuations can influence nearby regions, leading to cooperativity. The MD simulations indicate that above T_A, τ_{LC} is equal to the Maxwell characteristic time for viscous flow, τ_M. This suggests that the shear viscosity is governed by single excitations, giving an Arrhenius temperature dependence for the viscosity and an activation energy that is related to the effective bond strength. As the temperature is lowered below T_A, τ_M becomes increasingly larger than τ_{LC}, indicating that viscous flow becomes increasingly more cooperative, and the activation energy becomes increasingly larger with decreasing temperature. Experiments and MD simulations have indicated a correlation between T_A and the glass transition temperature, T_g, [11, 15].

While the crossover behavior in the viscosity has been experimentally observed and the value of T_A for different metallic liquids has been measured [15], clear experimental evidence for a structural connection has been difficult to obtain. A small change in the intensity of a low-q sub-peak in the second peak in the X-ray structure factor as a function of temperature has been found to correlate with T_A [16], but it occurs at a lower temperature. The weak scattering of the X-rays from the liquid structure could account for this difference, since the structural changes would need to be large enough to see them. Since electrons scatter more strongly, containerless measurements of the electrical resistivity, ρ, could reveal the structure/dynamics correlation. These measurements were made on $Zr_{64}Ni_{36}$ and $Cu_{50}Zr_{50}$ liquids using the EML facility located on the International Space Station, which allowed contamination with a container at high temperatures to be avoided [17]. As shown in Fig. 1, the temperature dependence of ρ suddenly increases below about T_A determined from the viscosity measurements (marked by the dashed vertical line), providing the strongest evidence to date for a change in structure that is correlated with the change in viscosity. Additionally, a surprising feature is observed that is not predicted by any existing theory of the resistivity of metallic liquids – a saturation or near saturation of the resistivity above T_A. While a saturation in the resistivity is known for most solids at very low cryogenic temperatures due to a vanishing of excitations that can scatter the electrons, this saturation is observed at very high temperatures where there should be an abundance of excitations. A possible explanation is that below T_A, the lifetime of the local liquid structure is much longer than the electron scattering times so that the supercooled liquid structure appears to be static with respect to the electrons. The resistivity changes in this temperature range are then largely due to electron/high frequency phonon scattering. With increasing temperature, both the length-scales and the structural lifetimes of the dynamically evolving local clusters decrease [11, 13, 14]. Near T_A, the mean electron scattering time becomes of order picoseconds, comparable with the structural relaxation times determined in our recent measurements of the Van Hove function [18]. The lifetimes of the pseudo-phonons of the small solid-like cluster regions then become too short to couple with the electrons. Moreover, the lifetime of the local cluster above T_A is too short to communicate with neighboring atoms, rendering the pseudo-phonons effectively localized. Both of these processes make the scattering mechanisms for the electrons ineffective, resulting in a near saturation of the electrical resistivity in a temperature region where viscous flow also becomes non-cooperative.

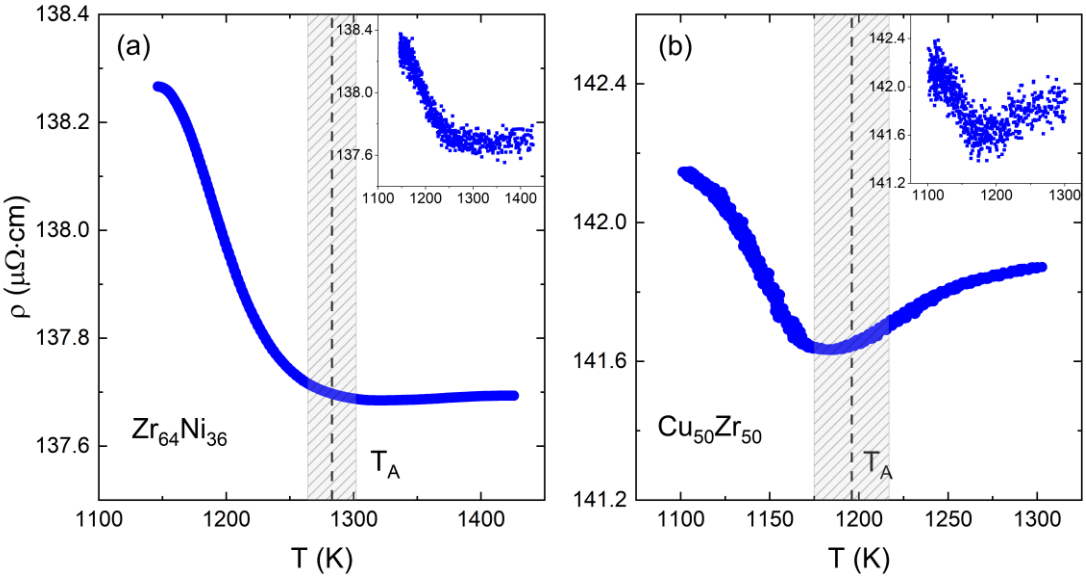

Fig. 1 The electrical resistivity, smoothed by 200-point averaging, as a function of temperature in liquid (a) $Zr_{64}Ni_{36}$ and (b) $Cu_{50}Zr_{50}$, showing near saturation at or above T_A. The shaded regions represent the uncertainties in T_A. The original unsmoothed data are shown in the insets. The data are reprinted with permission from ref. [17]. Copyright (2019) by the American Physical Society.

Influence of Stirring on Nucleation from a Supercooled Liquid

Nucleation is most commonly understood within the framework of the Classical Nucleation Theory (CNT) [19]. While there are some issues with the thermodynamic model used in CNT, the kinetic model appears to be correct for stoichiometric crystallization [20,21]. However, that is not true when the chemical compositions of the initial and final phases are different [22]. In that case the stochastic processes of interfacial attachment and long-range diffusion become coupled; the Coupled-Flux Model (CFM) model of nucleation was developed to treat this [23].

While kinetic Monte-Carlo studies support key predictions of the CFM [24], only recently were they confirmed experimentally by using the reduced gravitational environment of the ISS to investigate changes in the nucleation rate with stirring [25]. For small levels of stirring the nucleation rate of a phase with a different composition than the liquid is controlled by the coupled stochastic processes of interfacial attachment and long-range diffusion. The need for long-range diffusion decreases with increasing stirring rates and the CFM predicts that the nucleation rate should increase. There should be little effect of stirring on the nucleation rate of crystal phases that have the same chemical composition as the liquid. To investigate this, maximum undercooling measurements were made as a function of stirring for a Vit 106 liquid that crystallizes to phases with a different chemical composition than that of the liquid, and for $Cu_{50}Zr_{50}$ and $Ti_{39.5}Zr_{39.5}Ni_{21}$ liquids for which the nucleating phases have the same composition. The heating voltage and positioning voltage of the sample are decoupled to some extent in the electromagnetic levitation (EML) facility aboard the ISS (ISS-EML). For these experiments, different levels of stirring were achieved by different combinations of the positioner and heating voltages.

As shown in Fig. 2 the dynamical pre-factor for nucleation, A^*, increases as the maximum shear rate increases (which scales with the level of stirring) in the Vit 106 liquid. This indicates that the steady-state nucleation rate, I^s, ($I^s = A^* \exp(-W^*/k_BT)$ where W^* is the critical work of cluster formation) also increases, as predicted from the CFM. While, as expected, the influence of stirring is small for nucleation in the $Cu_{50}Zr_{50}$ and $Ti_{39.5}Zr_{39.5}Ni$, liquids (not shown here), what is surprising is a small decrease in the nucleation

rate with increasing shear rate for the $Ti_{39.5}Zr_{39.5}Ni_{21}$ liquid. Earlier studies have shown that the nucleation of a metastable icosahedral phase is catalyzed by icosahedral ordering in that liquid [26]. The decreasing nucleation rate with increased stirring might, therefore, indicate that stirring disrupts that ordering. This should be investigated further in future studies.

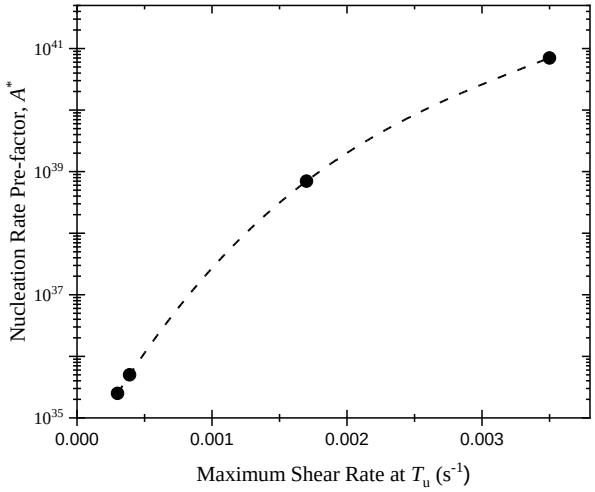

Fig. 2 The pre-factor for the nucleation rate as a function of the maximum shear rate at the maximum undercooling temperature of liquid Vit106 ($Zr_{57}Cu_{15.4}Ni_{12.6}Al_{10}Nb_5$), processed in vacuum using the ISS-EML. The dashed line is included as a guide to the eye. (Adapted from Fig. 2 in [25]).

Influence of convection on phase selection and the kinetics of phase transformation

When we address structural evolution and solidification physics issues, understanding phase selection is one of the pillars of the key space materials science topics [1]. Rapid solidification of Fe-Cr-Ni stainless steels [27] initially involves formation of metastable ferrite with a subsequent rapid transformation to the equilibrium austenite. Transformation kinetics, phase selection and microstructural evolution in this industrially important system are strongly influenced by both undercooling and convection.

The ISS-EML facility has as one of its chief attributes the ability to decouple positioning and heating of the sample through superposition of the levitation field [3]. Since thermophysical properties can be readily measured using the ISS-EML [28-29] a broad range of convection levels are achievable – spanning behavior from laminar to turbulent [30-31] as seen in Fig. 3(a) where magnetohydrodynamic (MHD) model predictions are used to guide the selection of processing conditions. Fig. 3(b) shows the corresponding incubation delay between formation of ferrite and austenite as a function of undercooling. For each stirring condition, characterized by the observed melt shear, the delay decreases significantly with undercooling. The stirring conditions are indicated by lines where red lines show ground-based electrostatic levitation (ESL) tests at zero melt shear, dotted red for ESL with Marangoni convection shear of $\gamma = 15\ s^{-1}$, blue lines show ground EML tests at $\gamma = 450\ s^{-1}$, and intermediate points correspond to the space convection settings shown in Fig. 3(a). Note that turbulent flow results approach ground EML and laminar

flow results approach ground ESL with Marangoni convection. Comparing stirring conditions, as convection increases the delay also significantly decreases.

This delay behavior is consistent with a growth competition model for phase selection [32-34] but, as described previously, CNT fails to explain this behavior. A new Retained Damage Model (RDM) was proposed that successfully predicts the influence of both undercooling and convection on delay[35-40] based on an analogy to hot-working. Damage is retained by the microstructure in the form of defects with an associated free energy. The faster the growth of the metastable phase (deeper undercooling), the more defects and the more retained free energy. The higher the melt shear (associated with increased convection), the more defects, and again, the more retained free energy. This retained damage within the metastable solid drives the subsequent transformation and results in a shorter incubation delay.

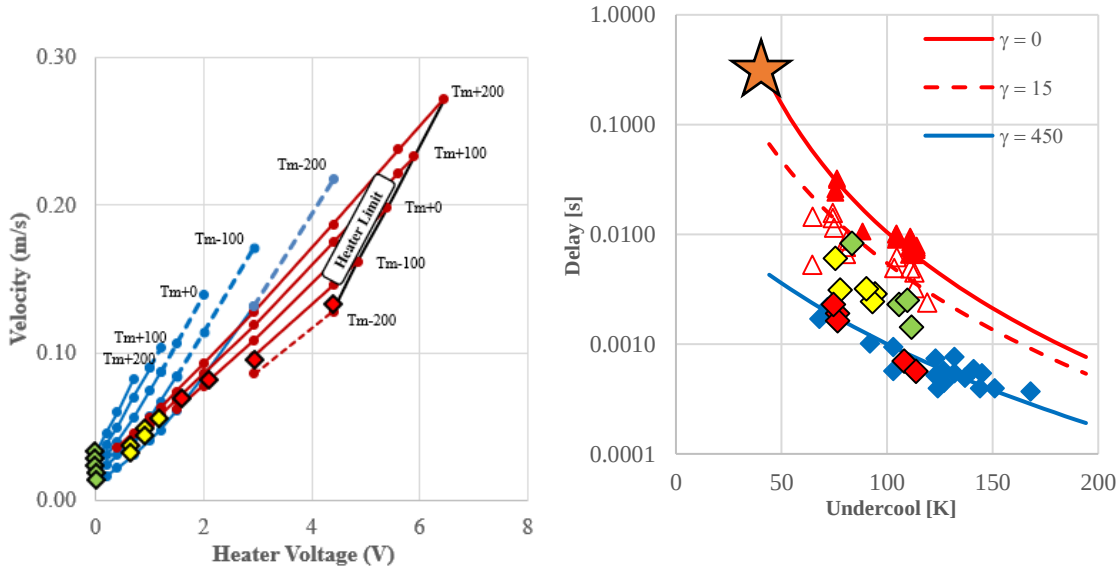

(a) (b)

Fig. 3 Space testing is important because on ground only the extremes in stirring may be investigated while in space, convection can be controlled over the entire continuum from laminar to turbulent flow.
(a) Convection range accessible using the ISS-EML facility by selecting a range of heater control voltage settings; points correspond to space run conditions in laminar (green), transition (yellow) and turbulent (red) flow regimes.
(b) Delay behavior as a function of undercooling and stirring condition

The lines in Fig. 3(b) correspond to RDM predictions at the given shear conditions. These results can also be presented in dimensionless form where $N_D = \tau/\tau_R$ and $N_M = \Delta G_T/\Delta G_R$ such that predictions from the RDM are presented in Fig. 4. The reference condition for normalizing delay and driving force is taken from an experimental determination of the maximum delay which is observed with zero stirring and at the minimum undercooling required to access the metastable phase (and thus minimum driving force) as defined by the phase diagram. This condition is indicated on Fig. 3(b) as an orange star. The observed slope of the dimensionless log-log plot is negative 3.992 ± 0.027 which compares favorably with the theoretical value of negative 4.0 from Equation 2.

$$\tau = \frac{128\,\pi\,k_B\,T\,\gamma^3 f(\theta)}{\beta}\left(\frac{\Omega}{N_A}\right)^2\left[\Delta G_T{}^{-4}\right] \qquad (2)$$

Here, τ is the delay, k_B the Boltzmann constant, T the transformation temperature, γ the surface energy, $f(\theta)$ the cluster geometry constant, Ω the molar volume, N_A Avogadro's number, β the attachment frequency, and ΔG_T the total retained free energy.

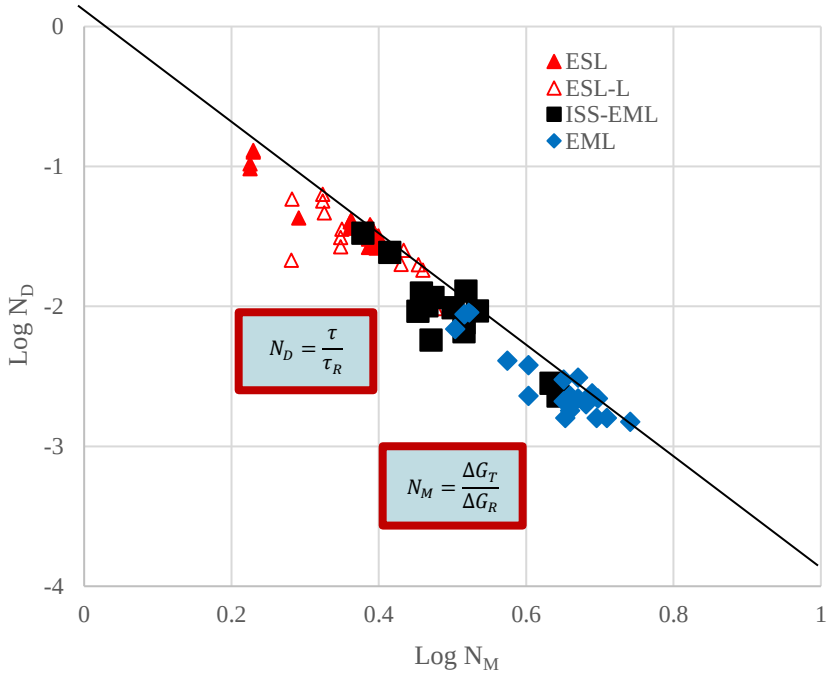

Fig. 4 Retained Damage Model performance comparing dimensionless delay time to dimensionless driving force.

Since undercooling and convection are extremely important in the control of industrial processes such as die casting, investment casting, directional solidification, welding and additive manufacturing, the new RDM prediction is a transformative advancement for use in modeling the production of high-quality, reliable products to optimize local properties and manage the development of defect structures both in space and in terrestrial industrial applications.

Metastable phase transformation by nucleation in the interdendritic liquid phase

Generally, upon solidification of a metastable phase in the undercooled melt the stable phase can nucleate either in the metastable solid or in the residual liquid phase within the mushy-zone. Metastable phase transformation will be dominated by the mechanism with the fastest kinetics, which may depend on the alloy system and the experiment conditions. As shown by the temperature-time profile as shown in Fig. 5(a), during rapid solidification of an electromagnetically levitated $Fe_{50}Co_{50}$ sample the temperature of the intermediate plateau, i.e. within the mushy-zone of primary metastable δ phase, is located near the liquidus temperature T_L^{δ}. Hence, the interdendritic liquid is undercooled by an amount corresponding to the difference between liquidus temperatures of stable γ and metastable δ phase, $\Delta T_{\gamma,\delta} = T_L^{\gamma} - T_L^{\delta}$. Upon the second recalescence step due to nucleation and growth of the stable γ phase, the temperature is further raised to the equilibrium liquidus temperature T_L^{γ} by which the primary dendrites are either

remelted or transformed into the stable phase. A model for the delay time for the conversion from metastable δ to stable γ phase considers the steady-state nucleation rate according to the classical nucleation theory and assumes heterogeneous nucleation of γ phase in the liquid at the surface of pre-existing dendrites of metastable δ phase [41, 42]. With the expanding mushy-zone during growth of the metastable phase the total number of potential heterogeneous nucleation sites rises with time. As growth velocity is increased with increasing undercooling, the number of nucleation sites and, therefore, the nucleation rate are rising faster as well. In addition, the interface area between dendrites and residual melt becomes larger with rising undercooling, which is due to a finer dendrite thickness and an increased fraction solid, thus leading to a higher number density of potential nucleation sites. Consequently, a critical nucleus of the stable phase is formed after a shorter period of time, i.e. the delay time is shortened as undercooling is raised. The evolution of the number of potential nucleation sites and, therefore, the heterogeneous nucleation rate over time is determined by the growth velocity v and the interface area estimated by the dendrite tip radius r of primary δ phase, which lead to the relation for the delay time [41]:

$$\Delta t \sim \left(\frac{\Delta H_f}{c_{p,L} \cdot K}\right)^{1/4} \cdot \left(\frac{r}{\Delta T_\delta \cdot v^3}\right)^{1/4} \cdot exp\left(\frac{1}{4}\,\frac{\Delta G^*_{het}}{k_B T_L^\delta}\right) \qquad (3)$$

Here $c_{p,L}$ is the specific heat of the liquid, ΔH_f is the latent heat of fusion of δ-phase and K is the attachment rate of atoms to the nucleus. The exponential term depends on the activation energy $\Delta G^*_{het} = (16\pi/3) \cdot \sigma^3_{S,L} \cdot f / \Delta G_V^2$ ($\sigma_{S,L}$: solid-liquid interfacial energy, f: catalytic potency factor, ΔG_V: Gibbs free energy difference per volume) for heterogeneous nucleation taken at the undercooling of the interdendritic, residual melt, $\Delta T_{\gamma,\delta} = T_L^\gamma - T_L^\delta$, and reflects the effect of alloy composition. Both growth velocity v and tip radius r are functions of the undercooling with respect to the liquidus temperature T_L^δ of metastable δ phase, $\Delta T_\delta = T_L^\delta - T_N$ (T_N: nucleation temperature of the undercooled melt) and are determined by models for dendritic growth in undercooled melts [43, 44].

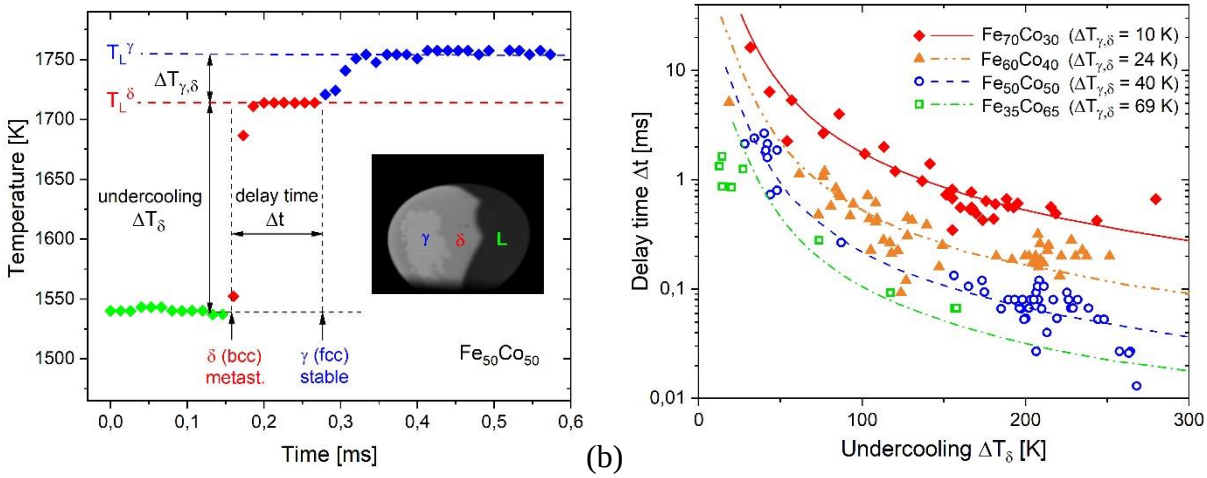

Fig. 5 (a) Temperature-time profile taken at the nucleation point and high-speed video image (insert) during double recalescence with primary metastable primary δ phase solidification and subsequent transformation into stable γ phase in ground-based electromagnetic levitation tests on $Fe_{50}Co_{50}$. (b) Measured delay times (symbols) as a function of the undercooling $\Delta T_\delta = T_L^\delta - T_N$ for different Fe-Co alloys obtained by high-speed video analysis in comparison to model prediction (lines) [41].

As shown in Fig. 5(b) the measured delay times plotted versus ΔT_δ are well described by the model in a wide range predicting an undercooling dependency according to $\left(r/\Delta T_\delta v^3\right)^{1/4}$. The nearly parallel curves are shifted towards shorter delay times with increasing Co concentration, which is mainly due to the enhanced temperature interval $\Delta T_{\gamma,\delta}$ according to the phase diagram [45] and, therefore to an increased Gibbs free energy difference acting as the thermodynamic driving force for phase transformation. As growth kinetics and pattern formation are generally influenced by fluid flow [46] the model also involves convection effects since the delay time explicitly depends on growth velocity and dendrite tip radius. In addition, fluid flow effects in particular in systems with strong solute partitioning can originate from the influence on the nucleation rate that is enhanced with increasing melt shear rate [25] as reported in the present article.

Atomization and evaluation of the solidification path

Impulse atomization (IA) is a drop tube-type containerless solidification technique where solidifying droplets experience high cooling rates and nucleation undercoolings. It consists of a transformation of a bulk liquid into a spray of liquid droplets that solidify rapidly during free fall by losing heat to the selected surrounding gas (usually N_2, Ar or He). The alloy is melted in a crucible using an induction furnace. Atomization is achieved by the application of a mechanical pressure (impulse) to the melt in order to push it through a nozzle plate with one or several orifices of known size and geometry. A liquid ligament emanates from each orifice, which in turn breaks up into droplets due to Rayleigh-type instabilities. The solidified powders are then collected in a beaker at the bottom of the tower. A detailed description of the process can be found in [47]. While EML can process one sample at a time, IA generates a range of droplets sizes per run (typically 50-1000 μm), giving a range of cooling rates and undercoolings. The cooling rate is a function of both the droplet size and the atomization gas and can reach up to ~10^5 K/s. Furthermore, solidification in free fall greatly minimizes convection within the samples. Thus, IA and EML are complimentary solidification technique for the evaluation of rapidly solidified samples.

Fig. 6(Fig. a) shows the microstructure of a 328 μm Al-36wt%Ni droplet atomized in helium. Solidification starts with the nucleation and growth of primary Al_3Ni_2 (light grey phase). Upon further cooling, a peritectic reaction occurs between the liquid and the primary phase to form Al_3Ni (dark grey phase). Due to the rapid solidification conditions, the peritectic transformation is however incomplete. The core of the primary dendrites remains as Al_3Ni_2. Finally, the remaining liquid solidifies as an α-Al– Al_3Ni eutectic (black areas). Some particles with diameters smaller than 180 μm exhibit a vastly different microstructure as shown in Fig. 6(b). The primary dendritic structure shows no sign of an incomplete peritectic reaction. Furthermore, compositional analysis indicate that the primary phase is actually Al_3Ni. Along with its morphology, this suggests that the high cooling rate experienced by the smaller droplets suppress the formation of Al_3Ni_2 and enables the direct nucleation of Al_3Ni from the liquid. Upon reaching the eutectic temperature, the remaining liquid then solidifies as α-Al– Al_3Ni. Neutron diffraction analysis of different droplet sizes also showed that the Al_3Ni_2 to Al_3Ni decreases as the particle size decreases (i.e. as the cooling rate increases) [47]. Furthermore, it was found that particles with diameters smaller than 275 μm contain some peaks that correspond to the formation of a quasicrystalline phase, known as D-phase. Löser and Shuleshova showed that this metastable forms 925 to 975 K [48], which corresponds to an undercooling of 150 to 200 K. Devred et al. found retained D-phase in gas-atomized particles with diameters smaller than 38 μm [49]. This indicates that the IA particles exhibiting peaks corresponding to the D-phase have experienced high primary phase undercooling and cooling rates during the solidification process. Fig. 6(c) shows selected synchrotron x-ray

microtomography slices of a 310 µm-diameter droplet atomized in helium. Similar to EML solidification in microgravity, several nucleation points are observed at the surface of the droplet, with dendrites growing towards the center of the sample.

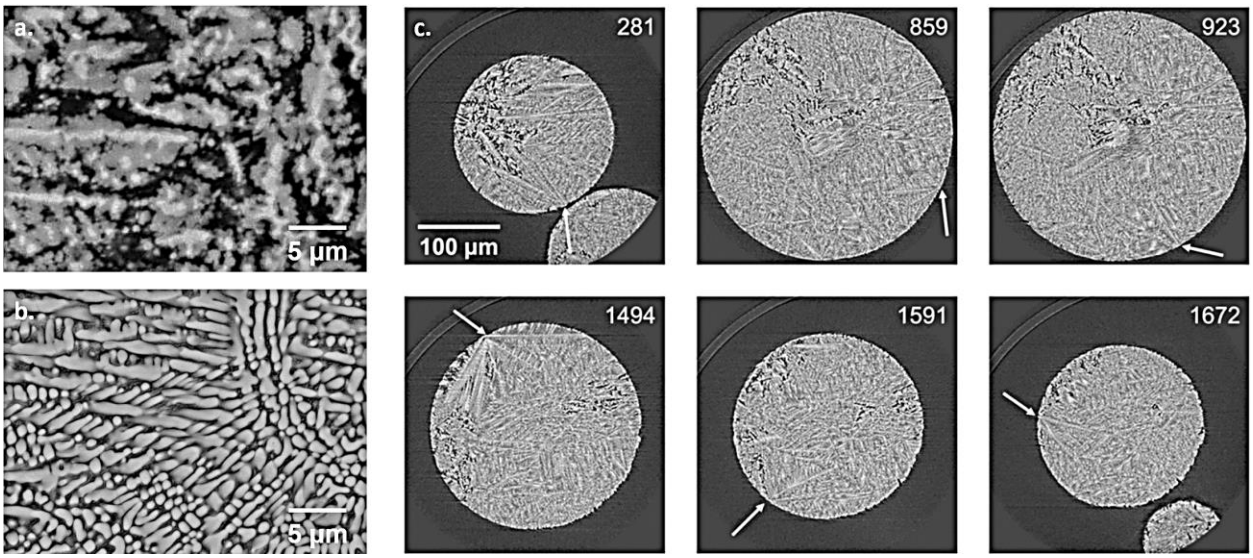

Fig. 6 BSE-SEM micrographs of Al-36wt%Ni ($Al_{80}Ni_{20}$) particles atomized in helium with diameters of (a) 328 µm and (b) 150 µm; (c) Selected synchrotron x-ray microtomography slices of a 310 µm Al-36wt%Ni ($Al_{80}Ni_{20}$) droplet atomized in helium. The arrows denote nucleation points at the surface of the droplets with primary dendrite arms growing towards the center of the droplet.

Modeling of the dendrite tip kinetics is key to understand the formation of microstructures in undercooled atomized systems. This is particularly true for multicomponent alloys for which only partial coupling with thermodynamic data was so far achieved. For this reason, a fully coupled dendrite tip kinetic model was recently developed and applied to a typical nickel-base alloy [50]. As shown in Fig. 7 the full diffusion profile of solute species is computed. It accounts for the full diffusion matrix in the liquid, hence explaining the existence of non-monotonous diffusion profiles [51]. Thermodynamic data are extracted from databases TCNI10 [52] and MOBNI5 [53]. Comparisons with classical approximations are discussed, including linearization of the multicomponent phase diagram, diagonal diffusion, approximation of the curvature undercooling, simplifications using multi-binary phase diagrams or a pseudo-binary phase diagram deduced from the former binary data. It is found that full coupling with thermodynamic data is essential for application of theories to multicomponent alloys. Extensions to implement a direct assessment to kinetics undercooling is under developments [$1], opening the way to revisit the interpretation of some microgravity data.

~~[$1] Hareland C., Guillemot G., Gandin Ch.-A., Voorhees P. W. The thermodynamics of non-equilibrium interfaces during phase transformations in concentrated multicomponent alloys, *Acta Materialia*, in press (2022)~~

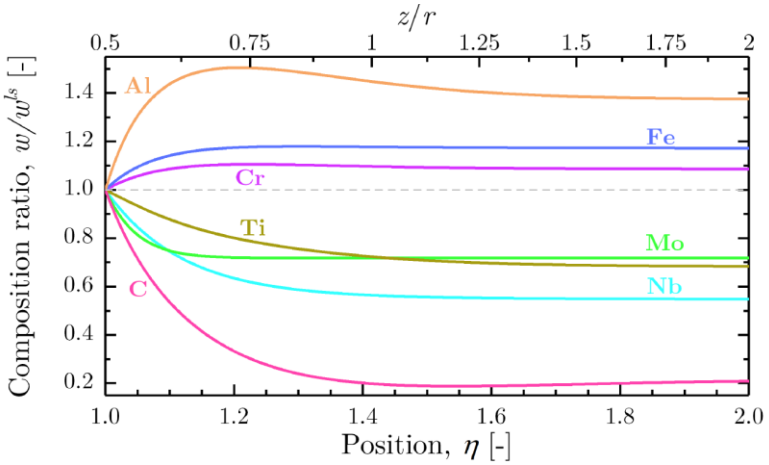

Fig. 7 Ratio between local liquid composition at paraboloidal coordinate η, $w(\eta)$, and liquid composition at the solid-liquid interface, w^{ls}, for the alloying elements of the IN718 alloy, with velocity v = 0.3 m s^{-1}. Coordinate η = 1 corresponds to the solid-liquid interface at the dendrite tip and coordinate η = 2 is located at a distance equal to 3r/2 from the tip of radius r [50].

Anomalous kinetics

From thermodynamical consideration, a monotonically increasing crystal growth velocity with increasing undercooling is expected in the crystallization of liquids, mixtures, and alloys [54]. By contrast to this general theoretical statement, Al-rich Al-Ni alloys show an anomalous solidification behavior in the “velocity *versus* undercooling" relationship [55, 56]: at low undercoolings, $\Delta T < 250K$, the velocity unexpectedly decreases with increasing undercooling. For higher undercoolings, $\Delta T > 250K$, the crystal velocity increases with increasing undercooling following the thermodynamically consistent trend seen in Fig. 8. In the light of measurements in microgravity with an Al-25at.% Ni alloy sample onboard the ISS, results confirm this anomalous behavior as an unexpected trend in solidification kinetics. It is also found that besides the anomalous growth behaviour, changes in the morphology, or recalescence growth front, occur. Indeed, the experimental results obtained using space high-speed camera coupled with subsequent metallographic analysis upon sample return have been compared with previous data gained on the ground [55, 56] using theoretical approaches based on statistical and analytical techniques. The experiments show different growth front morphologies in defined distinct ranges of undercoolings: planar front, scales, and dendrites, as displayed in Fig. 9. Scales are observed in the undercooling range where anomalous growth behavior is observed, i.e., for decreasing growth velocities with increasing undercooling. The scaled front consists of numerous nuclei ahead of crystal-liquid interface that occurs in the undercooling range featuring the negative slope for the crystal growth velocity at $\Delta T < 250K$. This unusual behavior is confirmed experimentally and explained theoretically using analytical solutions for the crystal growth front with the polydisperse ensemble of crystals nucleating ahead of the parent front[57, 58].

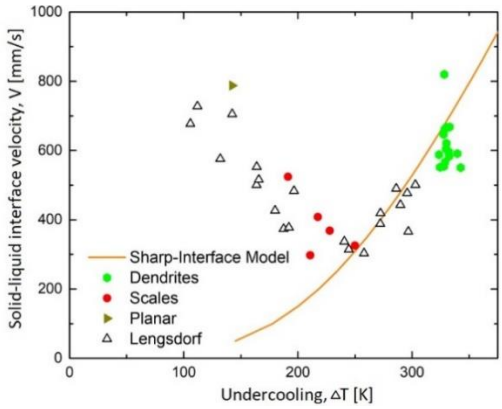

Fig. 8 Front velocity versus undercooling of the Al-35at.%Ni alloy. The empty black triangles represent the previously obtained data by Lengsdorf et al. [55, 56]. New data from the ISS-EML are marked with solid symbols, particularly a yellow triangle (planar), red circles (scales) and green hexagons (dendrites). The curve has been calculated with a sharp interface model [54], showing that beyond ΔT = 250K the expected velocity trend occurs. Calculations were made for the primary NiAl(B2)-phase. Experiments performed on ISS-EML, flight data 08.02.2018, cycle 5; data points were found 15.05.2019 from 16 cycles ISS-EML.

The scale distribution was analysed, and the results show that a lower number of larger scales forms with increasing undercooling. The analysis method [55, 56] for determining the growth velocities is not appropriate for this front morphology. The observed front is not a dendritic growth front, but a nucleation front. This is confirmed by the in-situ observation of the recalescence front using the high-speed camera as well as by metallographic evaluations on images of the microstructures shown in Fig. 10.

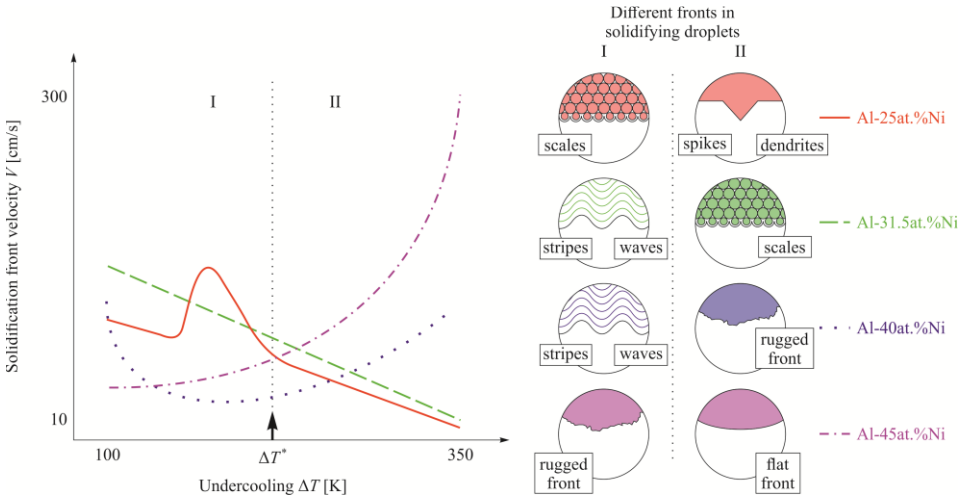

Fig. 9 Classification of solidification morphologies observed on the surfaces of Al-Ni droplets processed in EML on the Ground, under reduced gravity (in parabolic flights), and in microgravity (onboard the ISS). Classification is given by the behavior of solidification front velocity V as function of undercooling ΔT.

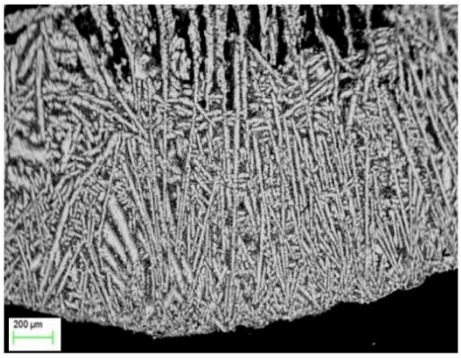

Fig. 10 Microstructure image of a sample of Al-35at.%Ni alloy solidified at $\Delta T = 189K$. This cross-section shows dendrites that are growing inwards the center of the sample

The measurements show multiple nucleation events forming the growth front in Fig. 10, confirming a mechanism that has been observed for the first time in Al-Ni alloys [57, 58] over the wide range of concentrations shown in Fig. 9. In particular, the experimental growth measurements and metallographic data directly demonstrate that the growth front does thus not consist of dendrite tips (as in usual rapid solidifying samples), but of newly forming nuclei propagating along the sample surface in a coordinated manner. Therefore, the measured velocity at small undercooling, $\Delta T < 250K$ is related to the nucleation evens but not to the growth phenomena [57, 59].

Directional solidification from levitated steel samples

Solidification processes are generally accompanied with liquid flow and thermomechanical deformations originating from the density difference between the liquid and the solid states as well as from thermal contraction [60]. As a benchmark experiment, deformation due to shrinkage is investigated during directional solidification of levitated droplets of different steel alloys in the frame of the European Space Agency (ESA) project entitled Chill Cooling for the ElectroMagnetic Levitator in relation with Continuous Casting of steels (CCEMLCC). A quenching device was developed, tested and implemented for chill solidification of levitated steel droplets for use in the ISS-EML facility

A Fe-0.9C-0.2Si (wt.%) steel droplet with average diameter 6 mm, was processed in the ISS such that the first few cycles were dedicated to thermophysical property measurements carried out in collaboration with the team of the THERMOLAB project at University of Ulm. They included liquid viscosity and surface tension as a function of temperature - both properties are key inputs for modelling activities relating to flow simulation within the mushy zone.

The final cycle was dedicated to chill cooling. By contacting the levitating liquid droplet with a Si_3N_4 plate positioned at one end of the sample cup holder, directional solidification took place. The long-term microgravity environment on ISS allowed complete solidification of the entire droplet under ideal and controlled conditions without external forces, which was not possible with parabolic flights. Fig. 11(a) shows the time evolution of the droplet shape during its solidification. The sample progressively elongates, starting from its initial equilibrium spherical shape and finally adopting a deformed shape. Comparisons with previously parabolic flight campaigns show that this behavior is presumably dominated by several parameters such as alloy composition, type of solidifying phase (ferrite or austenite), solidification interval between liquidus and solidus temperature and partitioning behavior of alloying elements. Samples processed in the ISS are expected to be returned to ground soon for inspections including metallography, optical imaging,

x-ray radiography, neutron diffraction and microprobe analyses. Meanwhile, modelling of both temperature and fluid flow velocity field during chill cooling have been carried out as shown in Fig. 11(b). The numerical simulation includes a thermohydraulic solution with surface tension and Marangoni convection, also accounting for solute mass and total mass conservations with shrinkage flow, the metal-gas boundary being dealt with a level set formulation [61, 62].

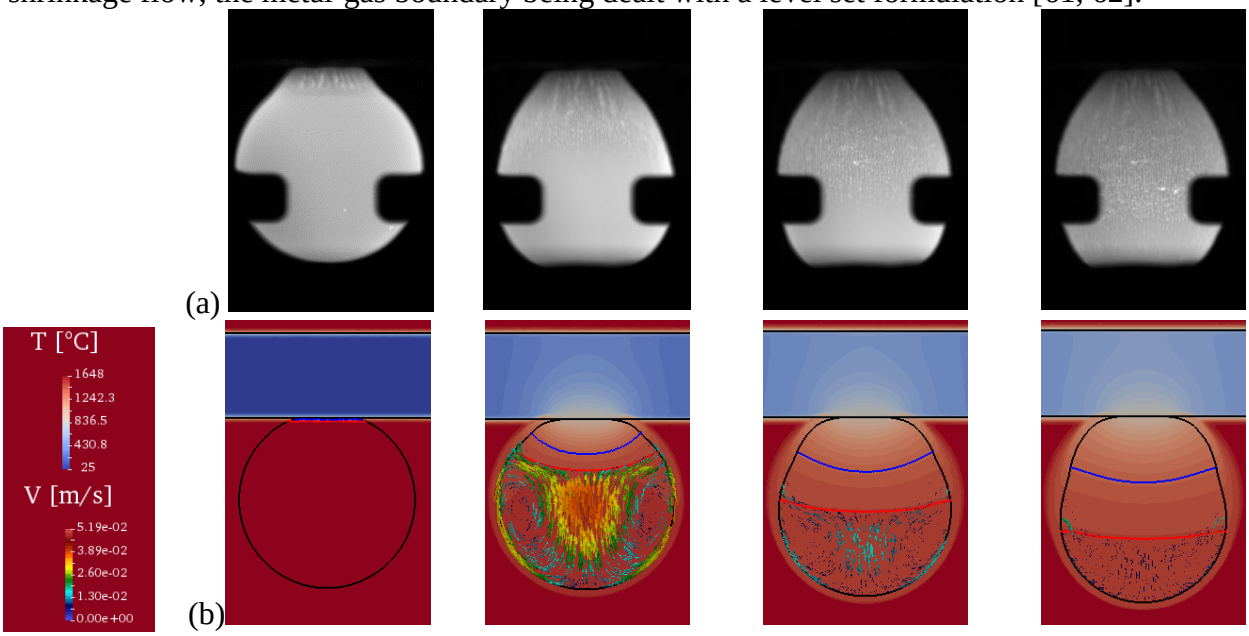

Fig. 11 Sequence of (a) video images during chill cooling of the Fe-0.9C-0.2Si (wt.%) sample (ID#20, Batch#2, ISS) with average diameter 6 mm and (b) thermohydraulic simulation with (round black contour) free liquid-gas boundary showing the temperature field in the (cold colors) cooling device, (hot colors) the metallic droplet and the surrounding gas, as well as (colored arrows) the velocity field and (red line) the start and (blue line) the end of solidification. Sample provided courtesy of ArcelorMittal (Maizières-lès-Metz, France).

Solidification of D2 steel, Fe-1.55C-11.8Cr-0.40Mn-0.80Mo-0.80V-0.30Si (wt.%), was also investigated. Fig. 12 (left) shows a scanning electron microscope image of a sample processed in microgravity during a parabolic flight. Solidification started at the contact surface between the sample and the quench plate. An array of columnar dendrites propagates away from the contact surface, covering about three quarters of the sample. Then, a columnar to equiaxed transition is observed, leading to the remaining part of the sample (on the opposite end of the quench plate) solidifying as equiaxed dendrites. Cooling rates are estimated from the measurement of the secondary dendrite arm spacing at various locations along the sample. A strong deformation of the initially spherical droplet is also observed along the direction of heat extraction (normal to the chill plate). D2 Tool Steels are ferritic at room temperature. However, due to the high carbon content, the first phase to form upon solidification is austenite. Previous studies on this alloy showed that rapid solidification can suppress the transformation from austenite to ferrite. Droplets generated by Impulse Atomization (102-105 K/s) were fully austenitic [63], while samples solidified using EML (10-50 K/s) showed 5-6% ferrite [64]. Neutron diffraction was carried out at Los Alamos National Laboratory (LANL) on the chill-cooled sampled shown in Fig. 12. Results of Rietveld analysis of the diffraction spectra yielded about 56% of austenite and 44% of ferrite. Neutron results showed strong variations of measured and fit peak intensities as a function of sample direction, indicating that the sample is textured. This is confirmed by the orientation contour plots

obtained after further analysis of the diffraction data. A strong texture is observed in austenite (red poles) while ferrite is random. This indicates that the columnar dendrites are mostly comprised of retained austenite while the equiaxed dendrites should mostly be ferrite. This is also coherent with the heat extraction process during solidification. The cooling rate is highest at the contact surface with the quench plate and then decreases away from the plate. Thus, it is expected that the microstructure is composed of retained austenite at the contact surface. The fraction of transformed ferrite should then increase as the local cooling rate decreases.

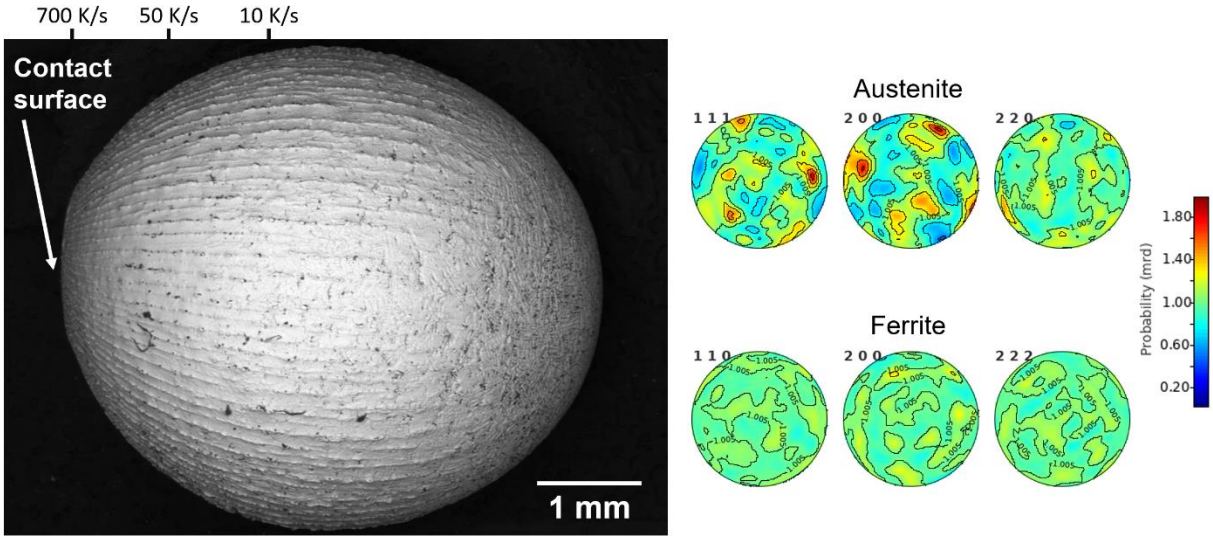

(a) (b)

Fig. 12 (a): SEM imaging of the surface of a chill-cooled D2 droplet. Columnar dendrites are propagating away from the contact surface. Further, a columnar to equiaxed transition is observed. (b): orientation contour plots obtained with neutron diffraction. Austenite has a stronger texture than ferrites.

Demixing of melts into liquids and solids

Monotectic alloys exhibit de-mixing of the melt into two liquids – L1 and L2. In some Cu alloys of industrial interest (examples are Co-Cu-Fe and Co-Cu shown in Fig. 13) the miscibility gap occurs below the liquidus as revealed by the shape of the phase diagram[65]. It is accessed on deeply undercooling the melt. In experiments, the metastable solvus is reached by rapid solidification in containerless levitation processing on Earth or in microgravity [66, 67], in free fall in a drop tube [68], by glass flux in a crucible [69] or by chill block quenching [70].

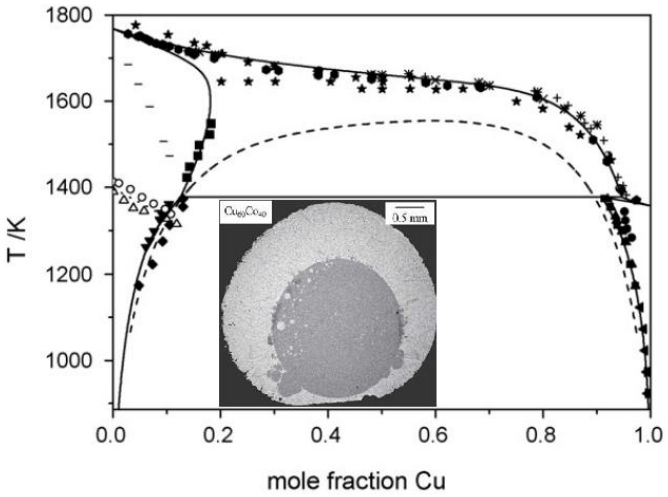

Fig. 13 The Co–Cu phase diagram optimised by CALPHAD; the metastable miscibility gap in the liquid is given by the dotted line and solid lines indicate experimental points from the literature. Inset: Cross sections of a $Cu_{60}Co_{40}$ sample processed using differential scanning calorimetry (DSC). Back scattered electron image where dark regions are Co rich and bright regions are Cu rich.

Due to high melt undercooling, the demixed liquid is solidified rapidly and the microstructure provides information about the metastable states of demixing. Cu-rich alloys have been extensively investigated to study the development of a dispersions of Co-rich liquid droplets seen in Fig. 14. The degree of melt convection has a strong influence on the dispersions, shown by experiments under different levels of convection in high magnetic field [71], during sounding rocket / parabolic flight or in terrestrial EML [68]. The release of latent heat by the Co-rich droplets upon solidification allowed observation of their movement in the melt *in situ* and thus allowed direct comparison of experimentally observed motion and predicted melt flow patterns using MHD modeling [72].

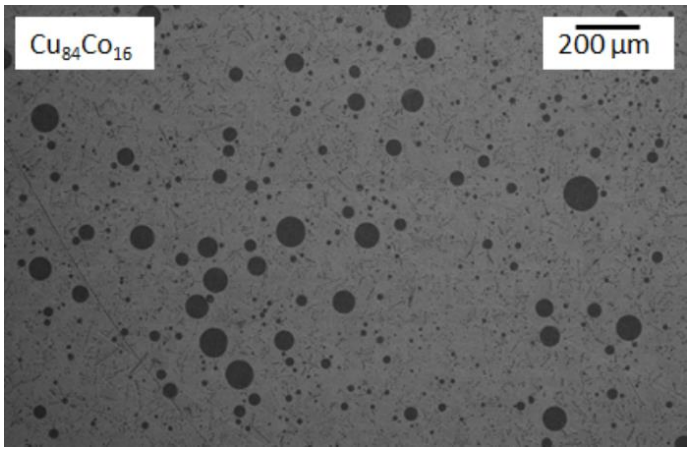

Fig. 14 Dispersion of Co-rich L1-droplets in the Cu-rich matrix L2. The alloy has been undercooled and solidified during parabolic flight in low gravity.

Reducing the convection while cooling the melt slowly on board of the ISS should allow the formation of a single drop of L1 surrounded by the L2 matrix, both spherical. Analysing the

oscillations of the inner droplet the liquid-liquid interfacial tension is measured which is a relevant parameter for the nucleation of L1 from the melt [66, 67]. Preliminary experiments on board of the TEXUS 44 rocket have provided values of the melt surface tension in agreement with previous data (1.21 N/m) and a first estimate of the L1-L2 interfacial tension (0.17 N/m at 1863 K) [67].

The de-mixing was studied in mm-sized spheres of Co-Cu alloys of various composition embedded in an oxide glass which were heated to the liquid state and cooled at constant rate directly into the cell of a DSC apparatus (inset of Fig. 13) [73]. Using the liquid-liquid interfacial free energy and the bulk free energy difference between L1 and L2 obtained by means of a new CALPHAD assessment of the Co-Cu phase diagram [65] to model the nucleation of phases, it has been established that the liquid-liquid separation is nucleation controlled and occurs without detectable undercooling below the binodal line, contrary to the nucleation of the Co-rich crystal phase which is undercooled more than three hundred degrees below the liquidus.

The measurement of the interfacial tension as a function of temperature requires additional future experiments on the ISS. Compared to a sounding rocket, which provides a microgravity time span of a few minutes, ISS experiments might be extended to a longer duration. In this case, the formation of a large Co-rich droplet in a Cu-rich shell might be accessible - which is the starting point for measurement of the interfacial tension.

Eutectic alloys solidify by demixing of the homogeneous melt into two solid phases. Near the thermodynamical equilibrium the two phases grow co-operatively leading to a regular lamellar structure. The solidification melt in the undercooling regime generally produces anomalous eutectic structures with outgrowth of a phase either in the form of dendrites or faceted crystals. These microstructures are influenced by convection. The phenomenon was investigated by means of various containerless processing techniques: electromagnetic levitation (EML), electromagnetic levitation under a static magnetic field (EML + SMF), and electrostatic levitation (ESL) employing the model line compound-line compound CoSi-$CoSi_2$ eutectic.[74, 75] Varied microstructures were achieved as a function of increasing undercooling occurring in the diverse techniques: primary dendrites or cells with regular eutectic, anomalous eutectic made of primary $CoSi_2$ with intergranular CoSi, complex shape of the primary phase embedding precipitates. The pathways to microstructure formation in EML samples as a function of undercooling were determined by X-ray diffraction [76, 77] including and evaluation of remelting behavior [78]. Further aspects of the solidification were revealed by both melt spinning (MS) and copper mould casting (CMC) [79] The first phase nucleating heterogeneously on the surface of the chilling block was most often the CoSi compound, as seen in Fig. 15, and then eutectic microstructure began to appear, However, in the adjacent melt more CoSi crystals were nucleated independently giving rise to an anomalous eutectic microstructure, with no coupled growth. Then a rod-like eutectic appeared followed by a transition to a zone where primary CoSi crystals were formed again by re-nucleation.

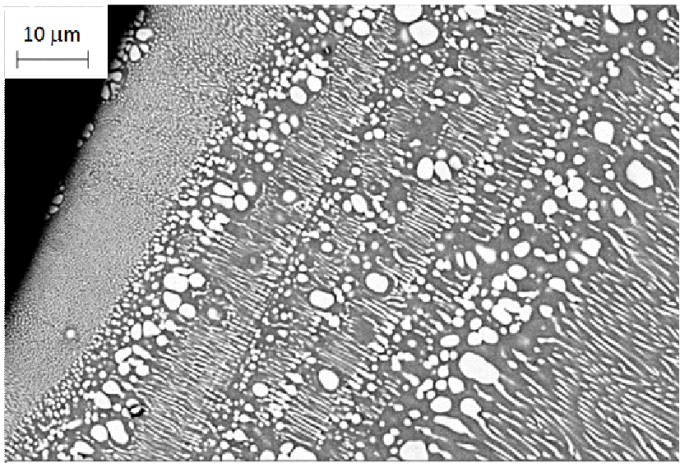

Fig. 15 Regular/anomalous eutectic bands in a mould cast cylinder of 2mm diameter of the Co-61.8at%Si alloy.

This banded microstructure was repeated four times before the regular rod-like eutectic filled the alloy. It is apparent that fluctuations in growth rate occur producing bands of the two types of eutectic. This stems from oscillations in the level of undercooling caused by the interplay of heat subtraction and recalescence. Melt spun ribbons confirmed the scenario in smaller samples. The microstructural features (eutectic spacing and band width) allows estimating the growth rates according to the Han-Trivedi model of band formation [80].

The directional heat extraction implied by copper mould casting and melt spinning apparently has overcome the convection and allowed to show the banding in the CoSi-$CoSi_2$ eutectic. The microstructure found in directional solidification has also practical counterpart for repairing processes. Microgravity experiments will be very relevant to gain better understanding of the phenomenon.

Process modeling

One of the repeating themes from all previous discussion is the need to control convection. Here, we utilize the unique attributes afforded by ISS-EML processing to decouple the levitation and heating function and then use the heating field to select the desired stirring conditions for a given experiment. Sometimes this is done to select the flow regime over the range from laminar to turbulent flow; sometimes to minimize stirring; but in all cases to use convection as a quantifiable, controlled experimental parameter. As shown in Fig.3(a), magnetohydrodynamic modeling is used to evaluate stirring and melt shear as a function of experimental conditions and control convection to desired levels [79-82]. Differential evaporation from complex industrial alloys can also be monitored over the test duration to set experimental conditions to minimize the potential for unwanted compositional shifts for volatile components in the melt [83]. These models require an understanding of the melt thermophysical properties – a subject of a sister article as part of this ESA review series. One additional significant advantage for the ISS-EML facility is the ability to measure thermophysical properties in parallel with measurements on rapid solidification physics.[84]

KEY KNOWLEDGE GAPS

To produce materials that meet ever-higher specific requirements and performance, the solidification processing of materials has to be controlled with ever-increasing precision. It is foreseen that the materials of tomorrow will be optimized in their design, featuring tailored composition for their specific application, underpinning more efficient production conditions, enhancing utilization of scarce resources, and favoring cleaner and more sustainable processes. At the heart of these initiatives is an understanding that structural evolution during liquid-solid phase transition requires experimental validation of theoretical and applied models across a broad range of length scales.

Moving forward developments in alloy design and manufacturing processes are increasingly directed by numerical modelling and simulation – heading eventually for integrated computational materials engineering techniques. Besides accessing a robust material property database (which includes not only an understanding of measurement accuracy but also a statistically-based reporting of precision to allow quantification of reliability and performance variability), advancing the state of the art in model development requires a knowledge of how convection influences the coupled processes involved in momentum transport, heat transfer, and mass transfer with a focus on interfacial phenomena.

One major thrust will be advancing the development of process modeling capability supporting additive manufacturing with an eye toward developing in-space manufacturing, material reuse and recycling, and in-situ resource utilization capabilities to support the human exploration and colonization missions off-planet. Low earth orbit (LEO) offers a unique environment where surface tension driven, or Marangoni, flow may be studied by eliminating buoyancy and sedimentation effects and where sample exchange and sample return is readily accomplished. The ISS-EML facility allows for selection of the desired stirring conditions and provides an enabling and powerful tool for the advancement of knowledge in solidification physics across a wide range of experimental objectives and a diverse set of current, and future, metallic material classes.

DATA AVAILABILITY

All data is available through contact with the authors.

ACKNOWLEDGEMENTS

The authors wish to acknowledge collaborative support by team members from the Microgravity User Support Center (MUSC) through access to the ISS-EML facility which is a joint undertaking of the European Space Agency (ESA) and the German Aerospace Center (DLR). The authors would also like to acknowledge funding for the following projects: NASA grant 80NSSC21K1649 for QUASI at Washington University, ESA MAP AO 2004-017 for CCEMLCC at Mines Paris and DLR Köln, the Natural Science and Engineering Research Council of Canada for NEQUISOL and CCEMLCC at University of Alberta, NASA grant 80NSSC19K0256 for ELFSTONE at Tufts University, and at DLR Köln: ESA grant 4200014980 for MAGNEPHAS/PARSEC, ESA MAP AO 2009-959 for ICOPROSOL, ESA MAP AO 99-010 for CoolCop and ESA MAP AO 2009-0894 for LIPHASE.

AUTHOR CONTRIBUTIONS

All authors, D.M.M., L.B., P.K.G., C-A.G., A.K.G., H.H., K.F.K, M.K., J.V., S.C.V., and T.V., participated extensively in this review. All were involved with concept design, modeling and analysis, manuscript writing, manuscript editing. D.M.M., L.B., P.K.G., C-A.G., H.H., K.F.K, M.K., and T.V are funded investigators.

COMPETING INTEREST

The authors declare no competing interests

References

1. Akamatu S., et al., White Paper #06: Materials Science, **ESASciSpaceE white paper** 1-48 (2021).
2. Hyers R.W., Matson D.M., KeltonK.F., and Rogers J.R., Convection in Containerless Processing, *Annals of the New York Academy of Sciences* **1027**, 474-494 (2004).
3. Seidel A., Soellner W., Stenzel C., EML – an electromagnetic levitator for the International Space Station, *J. Phys. Conf. Ser.* **327**, 012057 (2011).
4. Angell, C.A. Strong and Fragile Liquids. in Relaxation in Complex Systems. Springfield, VA: National Technical Information Service, U.S. Department of Commerce.(1984).
5. Martinez, L.M. and Angell C.A., A thermodynamic connection to the fragility of glass-forming liquids. *Nature* **410**(6829), 663-667 (2001).
6. Huang, D. and McKenna G.B., New insights into the fragility dilemma in liquids. *J. Chem. Phys.* **13**, 5621 (2001).
7. Novikov, V.N., Ding Y., and Sokolov A.P., Correlation of fragility of supercooled liquids with elastic properties of glasses. *Phys. Rev. E* **71**(6), 061501 (2005).
8. Mauro, N.A., Blodgett M., Johnson M.L., Vogt A.J. A Structural Signature of Liquid Fragility. *Nature Communications* **5,** 4616 (2014).
9. Kelton, K.F., Kinetic and structural fragility - a correlation between structures and dynamics in metallic liquids and glasses. *Journal of Physics: Condensed Matter*. **29,** 023002 (2017).
10. Gangopadhyay, A.K., et al., Correlation of the fragility of metallic liquids with the high temperature structure, volume and cohesive energy. *J. Chem. Phys.* **146,** 154506 (2017).
11. Jaiswal, A., Egami T., Kelton K.F., Schweizer K.S., Zhang Y., Correlation between Fragility and the Arrhenius Crossover Phenomenon in Metallic, Molecular, and Network Liquids. *Phys. Rev. Lett.* **117,** 205701 (2016).
12. Fan, Y., Iwashita T., and Egami T., Crossover from localized to cascade relaxations in metallic glasses. *Phys. Rev. Lett.* **115**, (2015).
13. Iwashita, T., Nicholson D.M., and Egami T., Elementary Excitations and Crossover Phenomenon in Liquids. *Phys. Rev. Lett.* **110**(20), 205504 (2013).
14. Soklaski, R., Nussinov Z., Markow Z., Kelton K.F., Yang L., Connectivity of icosahedral network and a dramatically growing static length scale in Cu-Zr binary metallic glasses. *Phys. Rev. B* **87**, 184203 (2013).
15. Blodgett, M.E., Egami T., Nussinov Z., Kelton K.F., Proposal for universality in the viscosity of metallic liquids. *Scientific Reports* **5,** 13837 (2015).
16. Dai, R., Ashcraft R., and Kelton K.F., A possible structural signature of the onset of cooperativity in metallic liquids *J. Chem. Phys.* **148**(20), 204502 (2018).
17. Van Hoesen, D.C., et al., Resistivity Saturation in Metallic Liquids Above a Dynamical Crossover Temperature Observed in Measurements Aboard the International Space Station. *Phys. Rev. Lett.* **123,** 226601 (2019).
18. Ashcraft, R.W., et al., Experimental measurements of the temperature-dependent Van Hove function in a $Zr_{80}Pt_{20}$ liquid. *J. Chem. Phys.* **152**(7), 074506 (2020).
19. Kelton, K.F. and Greer A.L., Nucleation in Condensed Matter - Applications in Materials and Biology. Pergamon Materials Series, ed. R.W. Cahn. Amsterdam: Elsevier. 726 (2010).

20. Kelton, K.F. and Greer A.L., Test of classical nucleation theory in a condensed system. *Phys. Rev.* **B38**(14), 10089-10092 (1988).
21. Greer, A.L. and K.F. Kelton K.F., Nucleation in Lithium Disilicate Glass: A Test of Classical Theory by Quantitative Modeling. *J. Am. Ceram. Soc.* **74**(5), 1015-22 (1991).
22. Kelton, K.F., Kinetic model for nucleation in partitioning systems. *J. Non-Crystalline Solids* **274,** (1-3) 147 -154 (2000).
23. Kelton, K.F., Time-dependent nucleation in partitioning transformations. *Acta Mater.* **48**(8), 1967-1980 (2000).
24. Diao, J., Salazar R., Kelton K.F., Gelb L.D, Impact of diffusion on concentration profiles around near-critical nuclei and implications for theories of nucleation and growth. *Acta Mater.* **56**(11), 2585-2591 (2008).
25. Gangopadhyay, A.K., et al., Demonstration of the effect of stirring on nucleation from experiments on the International Space station. *Npj Microgravity* **7,** 31 (2021).
26. Kelton, K.F., Lee G.F., Gangopadhyay A.K., Hyers R.W., First X-ray scattering studies on electrostatically levitated metallic liquids: demonstrated influence of local icosahedral order on the nucleation barrier. *Phys. Rev. Lett.* **90**(19), 195504 (2003).
27. Matson D.M., Hyers R. W., Volkmann T., and Fecht H.-J., Phase selection in the mushy zone: LODESTARS and ELFSTONE Programs, *J. Physics Conf. Ser.* **327**, 012009 1-7 (2011).
28. Matson D.M., Watanabe M., Pottlacher G., Lee G.W. and Fecht H.-J., Thermophysical Property Measurement: A Call to Action, *International Journal of Microgravity Science and Application* **33**[3], 330301 1-7 (2016).
29. Matson D.M., Xiao X., Rodriguez J.E. and Wunderlich R.K., Preliminary Experiments Using Electromagnetic Levitation On the International Space Station, *International Journal of Microgravity Science and Application* **33**[2], 330206 1-11 (2016).
30. Matson D.M., Xiao X., Rodriguez J.E., Lee J., Hyers R.W., Shuleshova O., Kaban I., Schneider S., Karrasch C., Burggraff S., Wunderlich R., Fecht H.-J., Use of Thermophysical Properties to Select and Control Convection during Rapid Solidification of Steel Alloys using Electromagnetic Levitation on the Space Station, *JOM* **69**[8], 1311-1318 (2017).
31. Matson D.M., Hyers R.W., and Volkmann T., Peritectic Alloy Rapid Solidification with Electromagnetic Convection, *J. Japanese Society of Microgravity Applications* **27**[4], 238-244 (2010).
32. Matson D. M., Growth Competition during Double Recalescence in Fe-Cr-Ni Alloys, in Materials in Space – Science, Technology, and Exploration, MRS Symposium Proceedings Vol. 551, A. F. Hepp, J. M. Prahl, T. G. Keith, S. G. Bailey, and J. R. Fowler, eds., Materials Research Society, Warrendale PA, 227-234 (1999).
33. Rodriguez J.E., Kreischer C., Volkmann T., and Matson D.M., Solidification velocity of Undercooled Fe-Co Alloys, *Acta Materialia* **122,** 431-437 (2017).
34. Rodriguez J.E, and Matson D.M., Lateral Heat Flux during Remelt Growth into the Mushy-zone, *Acta Materialia* **129,** 408-414 (2017).
35. Matson D.M. and Xiao X., Identifying metastable interface potency limits during steel alloy transformations, *Materials Letters* **212,** 256-258 (2018).
36. Matson D.M., Xiao X., and Jeon S., Optimization strategies for identifying the controlling mechanism for solid-state transformation in FeCrNi during rapid

solidification, *IOP Conf. Series: Materials Science and Engineering* **529,** 012012 1-7 (2019).
37. Matson D. M., Chapter 14 – Influence of convection on phase selection, in *Metallurgy in Space: Recent results from the ISS*, Fecht H.-J. and Mohr M. eds. , Springer TMS Series, ISBN 978-3-030-89783-3, 299-314 (2022).
38. Matson D.M., Liu X., Rodriguez J.E., Jeon S., and Shuleshova O., Retained free energy with enhanced nucleation during electrostatic levitation of undercooled Fe-Co alloys, *Crystals* **11,** 1-10 (2021).
39. Matson D.M., Influence of induced convection on transformation kinetics during rapid solidification of steel alloys: The Retained Damage Model, *JOM* **72**[11], 4109-4116 (2020).
40. Matson D.M., Retained free energy as a driving force for phase transformation during rapid solidification of stainless steel alloys in microgravity, *npj Nature - Microgravity* **4:22,** 1-6 (2018).
41. Kreischer, C., and Volkmann, T. Transformation kinetics of the metastable bcc phase during rapid solidification of undercooled Fe-Co alloy melts. *Materialia* **20**, 101211 (2021).
42. Kreischer, C. Crystallization and transformation of metastable phases in undercooled metallic melts, *PhD Thesis*, Technical University of Aachen (RWTH), Aachen, Germany, (2022).
43. Lipton, J., Kurz and W., Trivedi, R. Rapid dendrite growth in undercooled alloys. *Acta Metall*. **35** (4)**,** 957-964 (1987).
44. Boettinger, W. J., Coriell, S. R. and Trivedi, R. Application of dendrite growth theory to the interpretation of rapid solidification microstructures. *Rapid Solidif. Process. Princ. Technol.* **IV**, 13-26 (1988).
45. Rodriguez, J. E., and Matson, D. M. Thermodynamic modeling of the solidification path of levitated Fe–Co alloys. *Calphad* **49,** 87-100 (2015).
46. Kurz, W., Rappaz, M. and Trivedi, R. Progress in modelling solidification microstructures in metals and alloys. Part II: dendrites from 2001 to 2018. *Int. Mat. Rev.* **66** [1], 30-76 (2021).
47 Ilbagi A. and Henein H., 3D Quantitative Characterization of Rapidly Solidified Al-36 Wt Pct Ni, *Metall. Mater. Trans. A* **45**[4], 2152–2160 (2014).
48. Löser W., and Shuleshova O., Nucleation and Solidification Kinetics of Metastable Phases in Undercooled Melts, in *Solidification of Containerless Undercooled Melts*, John Wiley & Sons, Ltd, 187–212 (2012).
49. Devred F., Reinhart G., Iles G. N., Dahlborg U. and Calvo-Dahlborg M., ESRF Experimental report HS-3612 (2009).
50. Guillemot G., Senninger O., Hareland C., Voorhees P.W., Gandin Ch.-A., Thermodynamic coupling in the computation of dendrite growth kinetics for multicomponent alloys, *CALPHAD* (2022) *in press*.
51. Hunziker O., Theory of plane front and dendritic growth in multicomponent alloys, *Acta Materialia* **49,** 4191–4203 (2001).
52 Thermocalc database TCNI10 \Ni-Alloys v10.0, Thermo-Calc Software AB, Sweden (2021).
53 Thermocalc database MOBNI5 \Ni-Alloys Mobility v5.1, Thermo-Calc Software AB, Sweden (2021).

54 Galenko P.K. and Jou D., Rapid solidification as non-ergodic phenomenon, *Physics Reports* **818**, 1-70 (2019).
55 Lengsdorf R, Galenko P.K. and Herlach D.M. Measurement of dendrite growth on Al-Ni alloys in reduced gravity, in: European rocket and balloon programmes and related research ed. H Lacoste (Noordwijk: European Space Agency Communication Production Office) (2009).
56 Lengsdorf R., Holland-Moritz D., and Herlach D.M. Anomalous dendrite growth in undercooled melts of Al–Ni alloys in relation to results obtained in reduced gravity *Scripta Materialia* **62**, 365-67 (2010).
57 Herlach D.M., Burggraf S., Reinartz M., Galenko P.K., Rettenmayr M., Gandin Ch.-A., Henein H., Mullis A., Ilbagi A., Valloton J., Dendrite growth in undercooled Al-rich Al-Ni melts measured on Earth and in Space, *Physical Review Materials* **3**, 073402 1-7, (2019).
58 Reinartz M., Kolbe M., Herlach D.M., Rettenmayr M., Toropova L.V., Alexandrov D.V., Galenko P.K.., Study on Anomalous Rapid Solidification of Al-35 at%Ni in Microgravity. *JOM* **74,** 2420-2427 (2022).
59 Galenko P.K., Alexandrov D.V., Tolopova L.V., Assadi H., Reinartz M., Paul P., Fang Y., Rettenmayr M., Anomalous kinetics, patterns in recalescence, and final microstructure of rapidly solidifying Al-rich Al-Ni alloys. *Acta Materialia* (2022) submitted for publication.
60. Zhang Sh., Guillemot G., Gandin Ch.-A., Bellet M. A partitioned two-step solution algorithm for concurrent fluid flow and stress-strain numerical simulation in solidification processes. *Metall. Mater. Trans. B* **52**, 978-995 (2021).
61. Aalilija A., Gandin Ch.-A., Hachem E. On the analytical and numerical simulation of an oscillating drop in zero-gravity. *Computers and Fluids* **197**, 104362, (2020).
62. Aalilija A., Gandin Ch.-A., Hachem E. A simple and efficient numerical model for thermal contact resistance based on diffuse interface immersed boundary method. *International Journal of Thermal Sciences* **166**, 106817, (2021).
63. Delshad Khatibi P., Phillion A.B., and Henein H., Microstructural investigation of D2 tool steel during rapid solidification, *Powder Metall.*, **57**[1], 70–78, (2014).
64. Valloton J., Herlach D.M., Henein H., and Sediako D., Microstructural Quantification of Rapidly Solidified Undercooled D2 Tool Steel, *Metall. Mater. Trans. A* **48**[10], 4735–4743 (2017).
65 Palumbo M., Curiotto S., Battezzati L. Thermodynamic analysis of the stable and metastable Co–Cu and Co–Cu–Fe phase diagrams *CALPHAD-Computer Coupling of Phase Diagrams and Thermochemistry*, **30**, 171–178 (2006).
66. Kolbe M., Brillo J., Egry I., Herlach D. M., Ratke L., Chatain D., Tinet N., Antion C., Battezzati L., Curiotto S., Johnson E., Pryds N. H. Undercooling and Demixing of Copper-based Alloys *Microgravity Science and Technology*, **18** (3/4), 174-177 (2006).
67. Egry I., Ratke L., Kolbe M., Chatain D., Curiotto S., Battezzati L., Johnson E., Pryds N. H. Interfacial properties of immiscible Co–Cu alloys *J. Mater. Sci*. **45**, 1979-1985 (2010).
68. Kolbe M., Demixing of Cu-Co alloys showing a metastable miscibility gap, in: *Solidification of containerless undercooled melts*, eds.: D.M. Herlach, D.M. Matson, Wiley-VCH 51-67 (2012).
69. Cao C.D., Görler G.P., Herlach D.M., Wei B., Liquid–liquid phase separation in undercooled Co–Cu alloys, *Mater. Sci. and Eng.* **A325**, 503–510 (2002).

70. Battezzati L., Curiotto S., Johnson E, Pryds N.H. Undercooling and Demixing in rapidly solidified Cu-Co Alloys *Mater. Sci. and Eng.* ***A*** **449–451**, 7-11 (2007).
71. Zhang Y. K., Gao J., Yasuda H., Kolbe M., Wilde G., Particle size distribution and composition in phase-separated $Cu_{75}Co_{25}$ alloys under various magnetic fields, *Scripta Materialia* **82**, 5-8 (2014).
72. Lee J., Matson D.M., Binder S., Kolbe M., Herlach D.M., Hyers R.W., Magnetohydrodynamical modeling and experimental validation of convection inside electromagnetically levitated Co-Cu droplets, *Metall. Mater. Trans. B* **45**, 1018-1023 (2013).
73. Curiotto S., Pryds N. H., Johnson E., Battezzati L. Liquid-liquid phase separation and remixing in the Co-Cu system. *Metall. Mater. Trans. A*, **37**, 2361-2368 (2006).
74. Zhang Y.K., Gao J., Kolbe M., Klein S., Yang C., Yasuda H., Herlach D.M., Gandin Ch.-A. Phase selection and microstructure formation in undercooled Co–61.8 at.% Si melts under various containerless processing conditions. *Acta Mat.,* **61,** 4861–4873 (2013).
Jeon S. and Matson D.M., Formation of cellular structure on metastable solidification of undercooled eutectic CoSi 62 at%, *Crystals* **7**[10], 295 1-9 (2017).
Wang Y., Gao J., Kolbe M., Chuang A.C-P., Ren Y., and Matson D., Metastable solidification of hypereutectic Co_2Si-CoSi composition: microstructural studies and in-situ observation, *Acta Mat.* **142,** 172-180 (2018).
75 Jeon S.H., Kolbe M., Kaban V., String G., Cleaver A., Kaban I., Shuleshova O., Gao J. R., Matson D. M: Metastable solidification pathways of undercooled eutectic CoSi-$CoSi_2$ alloys, *Acta Mat.* **176,** 43-52 (2019).
76. Baker E., Jeon S., Shuleshova O., Kaban I., Wang Y., Gao J., Kolbe M., Sansoucie M., and Matson D.M., Dendrite remelting during rapid solidification of undercooled CoSi-$CoSi_2$ eutectic alloys quantified by *in situ* synchrotron X-ray diffraction *Scripta Materialia* **194**[3], 113645 1-6 (2021).
77. Fiore G.L., Quaglia A., Battezzati L., Banded regular/anomalous eutectic in rapidly solidified Co-61.8 at.% Si, *Scripta Mat.* **168**, 100–103 (2019).
78. Han S.H., Trivedi R., Banded Microstructure Formation in Off-Eutectic Alloys, *Metall. Mater. Trans. A* **31**, 1820–1832 (2000).
79. Lee J., Xiao X., Matson D. M., and Hyers R. W., Numerical Prediction of the Accessible Convection Range for an Electromagnetically Levitated $Fe_{50}Co_{50}$ Droplet in Space, *Metall. and Mater. Trans. B* **46**[2], 199-207 (2015).
80. Xiao X., Hyers R.W. and Matson D.M., Surrogate model for convective flow inside electromagnetically levitated molten metal droplet using magnetohydrodynamic simulation and feature analysis, *Int. J. Heat and Mass Transfer* **136** 532-542 (2019).
81. Xiao X., Lee J., Hyers R.W., and Matson D.M., Numerical representations for flow velocity and shear rate inside electromagnetically levitated droplets in microgravity, *npj Microgravity* **5:7** 1-7 (2019).
82. Baker E.B., Nawer J., Xiao X., and Matson D.M., MHD surrogate model for control of convection in electromagnetically levitated molten metal droplets processed using the ISS-EML Facility, *npj Microgravity* **6:9** 1-9 (2020).
83. Nawer J., Gossé S., and Matson D.M., Tracking evaporation during levitation processing of nickel-based superalloys on the ISS, *JOM,* **72**[9], 3132-3139 (2020).

84. Matson D.M., Watanabe M., Pottlacher G., Lee G.W. and Fecht H.-J., "Thermophysical Property Measurement: A Call to Action", *International Journal of Microgravity Science and Application*, **33**[3] 330301 1-7 (2016).

Figure Captions

Fig. 1 The electrical resistivity, smoothed by 200-point averaging, as a function of temperature in liquid (a) $Zr_{64}Ni_{36}$ and (b) $Cu_{50}Zr_{50}$, showing near saturation at or above T_A. The shaded regions represent the uncertainties in T_A. The original unsmoothed data are shown in the insets. The data are reprinted with permission from ref. [17]. Copyright (2019) by the American Physical Society.

Fig. 2 The pre-factor for the nucleation rate as a function of the maximum shear rate at the maximum undercooling temperature of liquid Vit106 ($Zr_{57}Cu_{15.4}Ni_{12.6}Al_{10}Nb_5$), processed in vacuum using the ISS-EML. The dashed line is included as a guide to the eye. (Adapted from Fig. 2 in [25]).

Fig. 3 Space testing is important because on ground only the extremes in stirring may be investigated while in space, convection can be controlled over the entire continuum from laminar to turbulent flow.
(a) Convection range accessible using the ISS-EML facility by selecting a range of heater control voltage settings; points correspond to space run conditions in laminar (green), transition (yellow) and turbulent (red) flow regimes.
(b) Delay behavior as a function of undercooling and stirring condition

Fig. 4 Retained Damage Model performance comparing dimensionless delay time to dimensionless driving force.

Fig. 5 (a) Temperature-time profile taken at the nucleation point and high-speed video image (insert) during double recalescence with primary metastable primary δ phase solidification and subsequent transformation into stable γ phase in ground-based electromagnetic levitation tests on $Fe_{50}Co_{50}$. (b) Measured delay times (symbols) as a function of the undercooling $\Delta T_\delta = T_L^\delta - T_N$ for different Fe-Co alloys obtained by high-speed video analysis in comparison to model prediction (lines) [41].

Fig. 6 BSE-SEM micrographs of Al-36wt%Ni ($Al_{80}Ni_{20}$) particles atomized in helium with diameters of (a) 328 μm and (b) 150 μm; (c) Selected synchrotron x-ray microtomography slices of a 310 μm Al-36wt%Ni ($Al_{80}Ni_{20}$) droplet atomized in helium. The arrows denote nucleation points at the surface of the droplets with primary dendrite arms growing towards the center of the droplet.

Fig. 7 Ratio between local liquid composition at paraboloidal coordinate η, $w(\eta)$, and liquid composition at the solid-liquid interface, w^{ls}, for the alloying elements of the IN718 alloy, with velocity v = 0.3 m s^{-1}. Coordinate η = 1 corresponds to the solid-liquid interface at the dendrite tip and coordinate η = 2 is located at a distance equal to 3r/2 from the tip of radius r [50].

Fig. 8 Front velocity versus undercooling of the Al-35at.%Ni alloy. The empty black triangles represent the previously obtained data by Lengsdorf et al. [55, 56]. New data from the ISS-EML are marked with solid symbols, particularly a yellow triangle (planar), red circles (scales) and green hexagons (dendrites). The curve has been calculated with a sharp interface model [54], showing that beyond ΔT = 250K the expected velocity trend occurs. Calculations were made for the primary NiAl(B2)-phase. Experiments performed

on ISS-EML, flight data 08.02.2018, cycle 5; data points were found 15.05.2019 from 16 cycles ISS-EML.

Fig. 9 Classification of solidification morphologies observed on the surfaces of Al-Ni droplets processed in EML on the Ground, under reduced gravity (in parabolic flights), and in microgravity (onboard the ISS). Classification is given by the behavior of solidification front velocity V as function of undercooling ΔT.

Fig. 10 Microstructure image of a sample of Al-35at.%Ni alloy solidified at $\Delta T = 189K$. This cross-section shows dendrites that are growing inwards the center of the sample

Fig. 11 Sequence of (a) video images during chill cooling of the Fe-0.9C-0.2Si (wt.%) sample (ID#20, Batch#2, ISS) with average diameter 6 mm and (b) thermohydraulic simulation with (round black contour) free liquid-gas boundary showing the temperature field in the (cold colors) cooling device, (hot colors) the metallic droplet and the surrounding gas, as well as (colored arrows) the velocity field and (red line) the start and (blue line) the end of solidification. Sample provided courtesy of ArcelorMittal (Maizières-lès-Metz, France).

Fig. 12 (a): SEM imaging of the surface of a chill-cooled D2 droplet. Columnar dendrites are propagating away from the contact surface. Further, a columnar to equiaxed transition is observed. (b): orientation contour plots obtained with neutron diffraction. Austenite has a stronger texture than ferrites.

Fig. 13 The Co–Cu phase diagram optimised by CALPHAD; the metastable miscibility gap in the liquid is given by the dotted line and solid lines indicate experimental points from the literature. Inset: Cross sections of a $Cu_{60}Co_{40}$ sample processed using differential scanning calorimetry (DSC). Back scattered electron image where dark regions are Co rich and bright regions are Cu rich.

Fig. 14 Dispersion of Co-rich L1-droplets in the Cu-rich matrix L2. The alloy has been undercooled and solidified during parabolic flight in low gravity.

Fig. 15 Regular/anomalous eutectic bands in a mould cast cylinder of 2mm diameter of the Co-61.8at%Si alloy.